Cavity Resonator Sensor and Temporal Signals Analysis for Object Detection in Granular Flows

Johan Nohlert, Thomas Rylander, and Tomas McKelvey

We present a microwave measurement system for detection of objects in granular media flowing through pipes. The system comprises a resonant cavity sensor operated in several high-order modes that yield spatially periodic sensitivities, and a microwave transceiver for high-speed S-parameter measurements. The temporal signatures resulting from the passage of an object and the temporal correlations of the noise caused by flow inhomogeneities are incorporated in a matched filter detector, which is shown to perform uniformly better than two reference power detectors. The input to the detectors is a real-valued signal obtained from the first principal component of the complex S-parameter data for each resonant mode. The detection capabilities of the system are evaluated by experiments where many object passage events are observed in granulates flowing down a vertical pipe. We study the detection of dielectric and metal objects of different size in microcrystalline cellulose pellets and glass beads. Reliable detection is demonstrated for metal objects down to 2-4 mm and Delrin objects down to 4-6 mm in diameter at a mass flow rate of 100 kg/h depending on the background material.

Index Terms—**Powders, flow measurement, microwave measurement, cavity resonator, matched filter, signal detection**

I. INTRODUCTION

Powders and granular materials are vastly encountered in many material processing industries such as the pharmaceutical, food, agriculture, cement, mineral processing and power generation industry [1]. Here, the use of in-line measurement techniques for material characterisation is an important tool for quality control and process optimisation. In this paper, we focus on one particular aspect of quality control, namely to detect undesirable objects in flowing granular materials. By undesirable objects, we mean discrete solid items that somehow contaminate the material of interest. Such objects may cause damage and wear of process equipment [2] or lead to quality issues and consumer hazards if objects appear in the final product, particularly for foods and pharmaceuticals [3]. An undesirable object is, in general, characterised either by an anomalous substance, or that its size is considerably larger than the background powder particles, or both these aspects simultaneously. Undesirable objects characterised by anomalous size can appear due to agglomeration of powder particles, or due to insufficient milling in cases where the powder is made by grinding a solid material. The problem to detect objects with anomalous size can be viewed as a special case of particle size measurement, a topic well studied

J. Nohlert (nohlertj@chalmers.se) is with ABB Corporate Research, Västerås, Sweden. T. Rylander and T. McKelvey are with the department of Electrical Engineering, Chalmers University of Technology, Gothenburg, Sweden.

in the literature. On-line particle size monitoring techniques include laser-based measurements [4], optical imaging [5] and particle collision analysis using piezo-electric sensors [6], mechanical resonances [7], acoustic techniques [8], and radar [9]. Recently, Sun et al. [10] developed a technique specifically for detecting the presence of large biomass particles in a background of wood dust during pneumatic conveying, based the vibrations and acoustic signals generated by the collisions between the particles and the pipe wall. However, since all the particles of interest do not necessarily collide with the wall at the location of the sensor, this approach is not suitable for applications aiming for complete detection of all objects. Industrial flow monitoring techniques should preferably be non-intrusive and allow for robust in-line operation in harsh industrial environments. In this respect, optical techniques have the drawback of being sensitive to dust adhering to the optical access windows. Acoustic and vibration-based methods often require probes that protrude into the material flow to obtain sufficient sensitivity and, furthermore, may be susceptible to ambient acoustic noise and vibrations.

This paper presents a microwave measurement technique for detecting objects in granular dielectric materials that flow down a vertical pipe by the aid of gravity, a situation that could occur in several of the above mentioned industries. The detection is here based on deviations in the complex permittivity $\epsilon = \epsilon' - j\epsilon''$ of the mixture of background powder and an object. Microwave sensors are widely used for industrial characterisation of liquid, solid and granular materials [11]–[13]. Among the available microwave sensor types, resonator sensors and especially cavities, provide the highest sensitivity to small variations in the permittivity [14]. Therefore, a cavity sensor is selected for the current measurement problem to enable the detection of small objects, possibly with low contrast in bulk permittivity. The presented microwave detection system comprises a cavity resonator sensor mounted in a pipe, a high speed microwave transceiver, and an algorithm for detecting objects in flowing granular materials based on the measured microwave transmission coefficient S_{21}. This microwave technique is non-intrusive and insensitive to dust deposition and to electromagnetic interferences, which makes it suitable for harsh industrial flow environments. The cavity sensor, which extends 700 mm along the flow direction and has a quadratic cross-section, supports (among others) the resonant modes TE_{101}-TE_{109}. These modes provide spatially periodic sensitivities (1 to 9 sensitivity maxima) in the direction of the flow, resulting in temporally periodic signals when an object or a flow inhomogeneity passes through the sensor. The idea pursued in this paper is to utilise these temporal signals for detection of objects using a matched filter detector

that incorporates the statistical properties of the flow and the specific signatures resulting from an object passage. Kobayashi et al. [15] used a similar sensor for measuring the mass flow of pulverised coal, which requires that the flow speed and material density are measured simultaneously. Their approach is based on a frequency tracking circuit to measure at high speed the resonant frequency of the mode TE_{119} where the flow speed is estimated based on the zero-crossing of the autocorrelation function of the time-varying resonant frequency shift. A similar approach to mass flow measurement using a single high-order resonant mode is presented in [16]. The current paper extends the principle to exploit the periodic spatial sensitivity of high-order resonant modes for particulate flow measurements, in the sense that multiple modes are used simultaneously to detect objects in the flow based on temporal signatures in the data.

An experimental set-up for gravity-fall powder distribution and automatised release of test objects into the flow is developed, which allows us to gather large amounts of data from many object passage events to evaluate the detection performance statistically. The detection performance is evaluated for spherical metal and dielectric objects in granulates consisting of microcrystalline cellulose pellets and glass beads, respectively. The uncertainty in the obtained detection ratios is estimated using the bootstrap method.

II. MEASUREMENT SYSTEM

A. Sensor design considerations

Fluctuations in the local powder density does to some extent propagate downstream with the flow velocity, so that the cross-correlation of the density at two points separated a certain distance in the direction of the flow, peaks at a time-lag corresponding to the transit time between the two points. This is the principle for cross-correlation based flow velocity measurements [17]. However, due to the continuous mixing of the density fluctuations resulting from various multiphase flow effects for granular media [18], it is expected that the degree of correlation decreases with the separation distance. The idea pursued in this paper is therefore to use a microwave sensor that measures over a sufficiently long flow distance, so that the correlation between the density at the two ends of the sensor has decayed substantially. The mixing (or de-correlation) of the flow occurring over this distance reduces the coherence of the temporal waveforms obtained from the sensor. On the contrary, a small target object that resembles a point perturbation in the permittivity that travels downstream with a certain velocity yields an output waveform that remains coherent and resembles the pure spatial sensitivity function of the sensor. Hence, we expect that the difference in the temporal signature between the powder flow and an object passage can be exploited to improve the detection by a matched-filter detector.

To find a suitable sensor length, we have performed experiments where we study the mixing effects in powders flowing down a vertical transparent pipe using video capture at 1000 frames per second. Based on a spatio-temporal analysis where we study the autocorrelation of the pixel intensity with respect to space and time lag (assuming that the pixel intensity corresponds to the local powder density), we conclude that a sensor length of 700 mm is sufficient to achieve a significant degree of de-correlation, for a pipe diameter of 36 mm and a range of powder materials and mass-flow rates of interest.

B. Microwave sensor

Our sensor, shown in Fig. 1, consists of a rectangular metal cavity with square cross-section and length $L_z = 700$ mm. The cavity connects to a circular stainless steel pipe with the inner diameter $D = 36$ mm (1.5 inch industrial standard) via circular holes in the cavity's end-plates in the xy-plane. A polycarbonate pipe with 2 mm wall thickness is used to guide the flowing material through the sensor. This pipe is fixed in the position where its inner surface coincides with the inner surface of the metal pipe by a shallow countersink in each of the cavity's end-plates and by contracting forces from the end-plates.

The cavity supports a number of resonant modes operating below the cut-off frequency $f_c^{TE_{11}}$ for the dominant waveguide mode TE_{11} in the circular pipe [19]. At frequencies below $f_c^{TE_{11}}$, the fields are evanescent in the inlet and outlet pipe sections which prevents radiation losses and yields a sensing region that is confined to the cavity section. Four coupling loops positioned according to Fig. 1 are used to enable measurements of transverse electric modes with dual polarisations, in particular the modes TE_{10m} and TE_{01m} as expressed in rectangular waveguide mode nomenclature. Although the sensor's four probes allow for simultaneous measurements with two different polarisations, we measure in this paper only at port 1 and 2 and leave port 3 and 4 terminated with $50\,\Omega$ loads.

Figure 2 shows the measured and simulated S-parameters of the sensor. These measurements are performed using a commercial vector network analyser (Rohde-Schwarz ZNBT8) and the simulations are done using a finite element model implemented in Comsol Multiphysics [20]. The resonances observed are indicated by the corresponding mode labels. Of particular interest are the modes TE_{101}-TE_{109}, whose computed electric fields are shown in Fig. 3.

We now consider a spatially varying complex permittivity perturbation $\Delta\epsilon = \epsilon - \epsilon_0$ relative to the air-filled cavity, which models the flowing powder and an undesirable object, possibly present at the same time. Assuming that the material under test is non-magnetic, i.e. $\mu = \mu_0$, the resulting perturbation Δf_m in the resonant frequency f_m^{res} of a mode m (relative to the resonant frequency of the air-filled cavity) is, to leading order, given by

$$\frac{\Delta f_m^{res}}{f_m^{res}} = -\frac{\int_V \Delta\epsilon |\boldsymbol{E}_m|^2 dv}{\int_V \left(\epsilon_0 |\boldsymbol{E}_m|^2 + \mu_0 |\boldsymbol{H}_m|^2\right) dv}. \tag{1}$$

Here, $\boldsymbol{E}_m$ and $\boldsymbol{H}_m$ are the electric and magnetic fields of mode m in the empty cavity and V is the cavity's volume [21]. Eq. (1) prescribes a spatial filtering of $\Delta\epsilon$ with the squared electric field as weighting function (i.e. $|\boldsymbol{E}_m|^2$ is the spatial sensitivity). Although Eq. (1) is exact only in the limit $\Delta\epsilon \to 0$, it is still qualitatively informative for larger perturbations
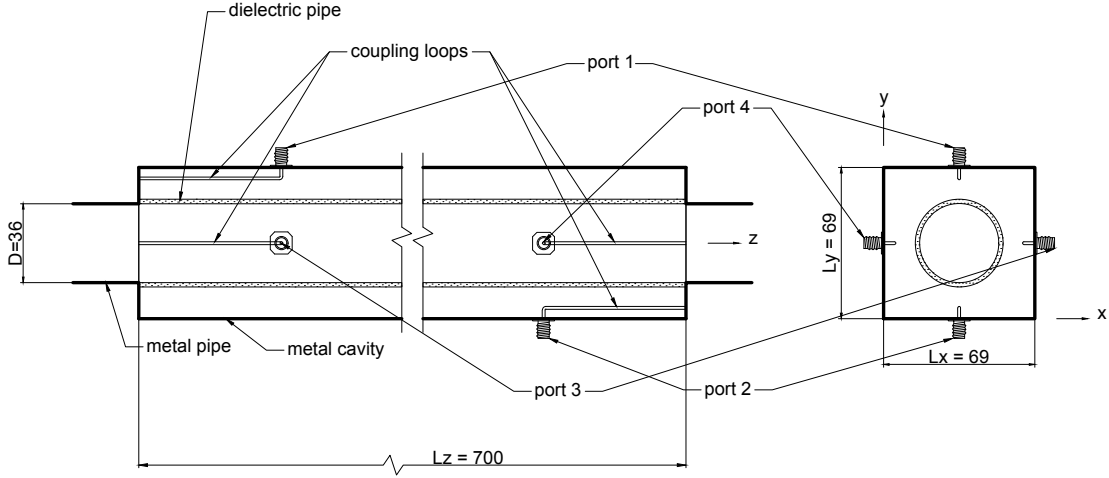
Figure 1. The cavity resonator sensor including coupling loops and associated ports. All dimensions are in millimeters.
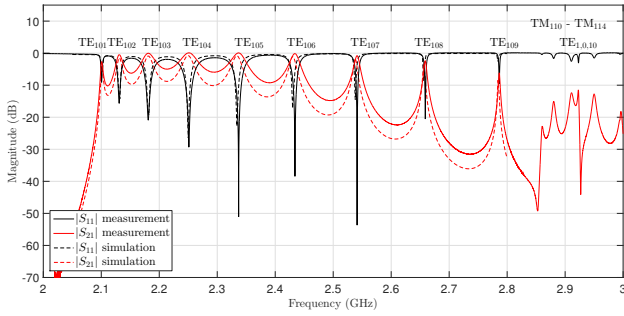

Figure 2. Measured and simulated S-parameters for the empty sensor.

since any increase in ϵ' will lead to a decrease in $\mathrm{Re}\{f_m^{\mathrm{res}}\}$, and any increase in dielectric loss ϵ'' yields an increase in $\mathrm{Im}\{f_m^{\mathrm{res}}\}$ (i.e. lowering of the Q-value) [21]. In this paper, we consider dilute powder flows with volume fractions below 1 % which, given the Maxwell-Garnett mixing rule, yields an effective permittivity that satisfies $\epsilon'_{\mathrm{eff}} < 1.03$ [22]. Hence the permittivity perturbations are generally small, which indicates that Eq. (1) is adequate for modelling how powder flow inhomogeneities and objects will affect the observed temporal signatures in the sensor data.

As seen in Fig. 3, the modes TE_{10m} have sinusoidal field variation in the axial direction z and relatively uniform field in the transverse plane. Consequently, their spatial sensitivity can be approximated by the function

$$h_m(z) = \begin{cases} A_m \sin^2\left(\frac{m\pi z}{L}\right) & z \in [0, L] \\ 0 & \text{otherwise,} \end{cases} \quad (2)$$

where A_m is a real positive constant amplitude. A single particle traveling through the sensor with constant speed v will thus give rise to a resonant frequency that oscillates with time t according to $h_m(vt)$ as the particle passes the maxima and nulls of the electric field. The spatial frequency response associated with $h_m(z)$ is given by its Fourier transform

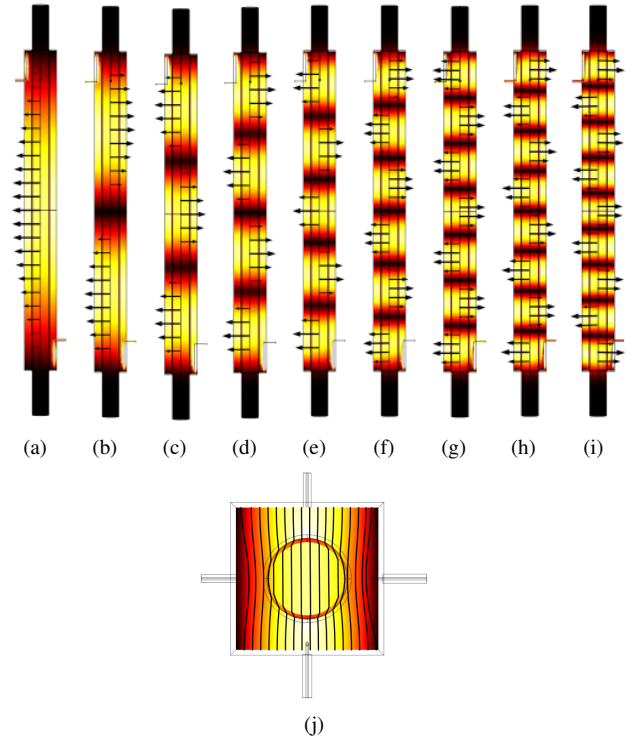$$H_m(k_z) = \int_{-\infty}^{\infty} h_m(z) e^{-\mathrm{j}k_z z} dz, \quad (3)$$

Figure 3. Electric field for the empty sensor with the field magnitude shown by color and the field direction by arrows or streamlines. (a)-(i): Field distribution in the yz-plane for the modes TE_{101}-TE_{109} in order from left to right. (j): Field distribution in the xy-plane, which applies to all the modes TE_{101}-TE_{109}.

which can be readily calculated although the result is omitted here for brevity. Figure 4 shows $h_m(z)$ and $|H_m(k_z)|^2$ for $m = 9$. It is seen that modes with periodic spatial sensitivity act simultaneously as bandpass and lowpass filters in the spatial domain. The output signal of such mode (i.e. the resonant frequency or a reasonably linear function thereof) is therefore mainly sensitive to one particular spatial frequency of the material that moves through the sensor, and to its average value. This principle is the basis for spatial filtering
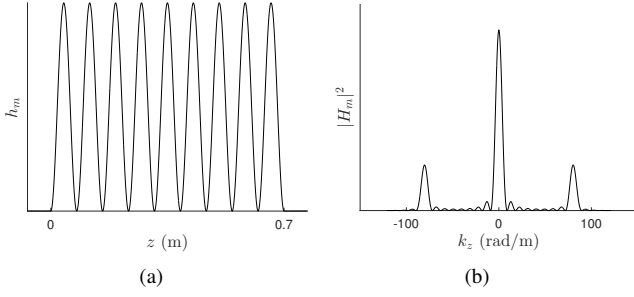
Figure 4. Ideal spatial sensitivity of mode $m = 9$ for $L = 0.7$ m. (a) With respect to the spatial coordinate z; (b) with respect to the spatial frequency k_z where the peaks at nonzero frequency occur approximately at $k_z = \pm 2\pi m/L$.

velocimetry [23]. A longer sensor yields a higher spatial frequency resolution which is manifested by more narrow-band peaks in $|H_m(k_z)|^2$. Furthermore, a longer sensor makes it possible to have a larger number of resonant modes in a given range of measurement frequencies of interest (2-3 GHz in our case).

A corresponding small metal object at a position $\boldsymbol{r}$ essentially removes a small part of the cavity volume which yields a resonant frequency perturbation that is approximately given by [21]

$$\frac{\Delta f_m^{\mathrm{res}}}{f_m^{\mathrm{res}}} = \frac{V_{\mathrm{obj}}\left(\mu_0|\boldsymbol{H}_m(\boldsymbol{r})|^2 - \epsilon_0|\boldsymbol{E}_m(\boldsymbol{r})|^2\right)}{\int_V \left(\epsilon_0|\boldsymbol{E}_m|^2 + \mu_0|\boldsymbol{H}_m|^2\right) dv}. \qquad (4)$$

Hence, the resonant frequency decreases when the metal object approaches a position of maximum electric field and it increases when the object approaches a position of maximum magnetic field. We thus conclude that the temporal signature of a metal object passage is different from that of a dielectric object in general.

C. Measurement electronics

The measurement response of the sensor is acquired using a custom microwave transmitter and receiver instrument that enables a high measurement speed. This instrument is based on a heterodyne transmitter and receiver controlled by an FPGA and it measures the amplitude and phase of sinusoidal signals transmitted through the sensor between ports 1 and 2 together with the coaxial cables that connect the measurement instrument to the sensor. The frequency of the stimulus signal is repeatedly swept over a discrete set of measurement frequencies with a minimum frequency separation of 5 MHz. This electronics yields a dynamic range of approximately 50 dB, but we emphasise that the instrument noise is overshadowed by the variability in the data due to random material movement and hence, the level of instrument noise is not a limiting factor for the object detection capability. The instrument is programmed before each experiment to measure at three adjacent frequency points around the expected mean value of each resonant frequency, which depends on the intended material loading. After the data is collected, we select for each mode one measurement frequency f_m among the three adjacent frequencies that yields the largest variance in the data during the material flow. As the sensitivity and hence the data variance is maximised at

resonance, the selected measurement frequency f_m is as close as possible to the average $\bar{f}_m^{\mathrm{res}}$ of the resonant frequency for mode m during powder flow for the particular experiment. The frequency sweeps are repeated at a rate of 500 sweeps per second and hence our effective sampling rate is $F_s = 500$ Hz. Further details on this electronics is given i [24].

The data obtained from the instrument are the raw numeric values from the A/D converter at the receiver. In the following, we use the complex data representation $w_m(t) = I_m(t) + \mathrm{j}Q_m(t)$ where $I_m(t)$ and $Q_m(t)$ are the in-phase and quadrature signal components at the measurement frequency f_m at time t. The measurement frequency f_m is chosen such that the mode TE_{10m} is excited. Thus, $w_m(t)$ is related to the complex transmission coefficient $S_{21}(f_m)$ at measurement frequency f_m upon normalisation by the transmitted signal's amplitude and phase. However, it should be emphasised that no calibration in the sense of physically connecting separate calibration standards to the instrument ports has been performed to compensate for delay and damping in cables or any internal characteristics of the transmitter and receiver. This implies that significant systematic errors are present in $w_m(t)$ if it is viewed as a representation of $S_{21}(f_m)$. Instead of addressing the calibration problem, we focus in this paper on the development of detection algorithms that can handle instrument calibration errors, including slow drifts.

III. SIGNAL PROCESSING

A. Measurement model

Given that the sensor acts as a spatial filter mainly in the axial direction z, the time-domain measurement response in the raw data for channel m can be modelled as

$$w_m(t) = a_m \int_0^L h_m(z)\Delta\epsilon(z,t)dz + b_m. \qquad (5)$$

Here, $\Delta\epsilon(z,t)$ is the deviation in the permittivity relative to air, and $h_m(z)$ is the spatial sensitivity given by Eq. (2). Furthermore, a_m and b_m are complex coefficients which account for the fact that the complex data $w_m(t)$ (which resembles S_{21}) is distributed over an elongated region in the complex plane. Thus, the size and orientation of the elongated data region is modelled by a_m and its center is represented by b_m. It should be noted that a_m and b_m may vary slowly in time due to e.g. variations in the material's moisture content and flow properties, or temperature variations influencing the measurement electronics. In the following, we assume that a_m and b_m are constant on the time-scale associated with the transit time for the material (powder or object) to pass through the sensor, which is represented by $\Delta\epsilon(z,t)$.

Equation (5) prescribes a linear relation between S_{21} and $\Delta\epsilon$ which is supported by the following argument: As the transmission response of a cavity can be well described by a pole-series model [25], we may write

$$S_{21} = \sum_k \frac{\beta_k}{f_m - f_k^{\mathrm{res}}} \approx C + \frac{\beta_m}{f_m - f_m^{\mathrm{res}}}$$

$$\approx C + \frac{\beta_m}{(f_m - \bar{f}_m^{\mathrm{res}})^2}\Delta f_m^{\mathrm{res}}. \qquad (6)$$

Here, β_k are the residues associated with the poles f_k^{res} which fluctuate due to background material movement while f_m is fixed. The first approximate equality applies because the pole f_m^{res} dominates the total response at the measurement frequency f_m. The second approximate equality is obtained as the first-order Taylor expansion with respect to $\Delta f_m^{\text{res}} = f_m^{\text{res}} - \bar{f}_m^{\text{res}}$ where $\bar{f}_m^{\text{res}}$ is the mean value of f_m^{res}. By invoking Eqs. (1) and (2), the linear spatial filtering relation between S_{21} and $\Delta\epsilon$ prescribed by Eq. (5) is established. The first-order Taylor expansion is accurate if the fluctuations Δf_m^{res} are small in comparison with the bandwidth of the resonant mode m when the flowing material is present.

In section III-B we present a pre-processing algorithm which aims to determine the coefficients a_m and b_m for each channel in order to map the raw data $w_m(t)$ onto a new data sequence $x_m(t)$ according to

$$x_m(t) = \text{Re}\left\{\frac{w_m(t) - b_m}{a_m}\right\}. \qquad (7)$$

The coefficients a_m and b_m are determined such that the direction of maximum variance in the complex plane for $w_m(t)$ (this direction usually corresponds to variations in the material density) is mapped onto the real part of $(w_m(t) - b_m)/a_m$. Hence, for sufficiently small real-valued permittivity perturbations and in absence of instrument noise, we have the relation

$$x_m(t) = \int_0^L h_m(z)\Delta\epsilon(z,t)dz. \qquad (8)$$

In the following, we assume that this pre-processing is adequately performed and hence we use the data $x_m(t)$ for all further estimation and detection tasks.

We assign a null hypothesis $\mathcal{H}$ to the situation where no object is present in the material flow, and an alternative hypothesis $\mathcal{K}$ to the event where a small object with random arrival time is present in the same material flow. In the idealised case where the powder and object travels with uniform speed v and no powder mixing occurs, we have the following model

$$\mathcal{H} : \Delta\epsilon(z,t) = w_\epsilon(z - vt) \qquad (9)$$
$$\mathcal{K} : \Delta\epsilon(z,t) = w_\epsilon(z - vt) + s_\epsilon(z - vt). \qquad (10)$$

Here, $w_\epsilon(z)$ is a spatial random process that represents the deviation in the permittivity of the powder at time $t = 0$. Furthermore, $s_\epsilon(z) = A\delta(z - z_{\text{a}})$ (where δ is the Dirac distribution) models the perturbation in the permittivity due to a small dielectric object whose arrival time is controlled by the uniformly distributed random variable z_{a}. Given the z and t dependence prescribed by Eqs. (9) and (10), Eq. (8) takes the form of a convolution. Under the assumption that the processes w_ϵ and s_ϵ are stationary and ergodic, the power spectrum of $x_m(t)$ under each hypothesis is given by

$$P_{x_m}(\omega|\mathcal{H}) = v^{-1}P_{w_\epsilon}(k_z)|H_m(k_z)|^2 \qquad (11)$$
$$P_{x_m}(\omega|\mathcal{K}) = v^{-1}\left(P_{w_\epsilon}(k_z) + P_{s_\epsilon}(k_z)\right)|H_m(k_z)|^2 \qquad (12)$$

where P_{w_ϵ} and P_{s_ϵ} denote the power spectra of w_ϵ and s_ϵ, respectively, and $k_z = \omega/v$. The impulse assumption for the target signal s_ϵ yields a power spectrum P_s which is flat over the relevant frequency band.

From a detection-theoretical point of view, it may seem natural to formulate a detector based on a hypothesis test that involves all available data in an analysis window containing, say, W consecutive samples from each of the M different channels [26]. For the analysis window to be larger than the passage time of an object, it is required that $W > F_sL/v$. For Gaussian distributed data, the joint likelihood function is parametrised by a covariance matrix of size $MW \times MW$ that encodes all correlations between mutual channels and relevant time-lags. Such covariance matrix however turns out to be rank deficient because all the channels observe the same underlying stochastic permittivity, although through different spatial filters, which prompts for regularisation to obtain a sufficiently well-conditioned covariance matrix estimate from data. Furthermore, the computational effort associated with estimation, inversion and multiplication of large covariance matrices may be prohibitive for real-time detection applications. Therefore, we consider an alternative approach where we seek to linearly combine the data from different channels according to

$$x[n] = \sum_{m=1}^{M} \alpha_m x_m[n] = \int_0^L h(z)\Delta\epsilon(z,t_n)dz, \qquad (13)$$

where the real-valued channel weights α_m are to be determined by a suitable criterion. Here, the discrete sample times are given by $t_n = nT_s$ with sampling interval $T_s = 1/F_s = 2\,\text{ms}$. The second equality in Eq. (13) is obtained by interchanging the order of summation and integration and using the following relation for the combined spatial filter

$$h(z) = \sum_{m=1}^{M} \alpha_m h_m(z), \qquad (14)$$

which has the corresponding frequency response

$$H(k_z) = \sum_{m=1}^{M} \alpha_m H_m(k_z). \qquad (15)$$

We now consider the problem to design the combined spatial filter $H(k_z)$ by choosing the coefficients α_m in order to make the signature of an object as prominent as possible in the combined data $x[n]$ for some given flow condition. We therefore seek to maximise the signal to noise ratio (SNR)

$$\text{SNR} = \frac{\int_{-\infty}^{\infty} P_{s_\epsilon}(k_z)|H(k_z)|^2 dk_z}{\int_{-\infty}^{\infty} P_{w_\epsilon}(k_z)|H(k_z)|^2 dk_z} = \frac{\boldsymbol{\alpha}^{\text{T}}\mathbf{A}\boldsymbol{\alpha}}{\boldsymbol{\alpha}^{\text{T}}\mathbf{B}\boldsymbol{\alpha}}, \qquad (16)$$

where $\boldsymbol{\alpha} = [\alpha_1, \ldots, \alpha_M]^{\text{T}}$, and

$$(\mathbf{A})_{mn} = \int_{-\infty}^{\infty} P_{s_\epsilon}(k_z)H_m^*(k_z)H_n(k_z)dk_z \qquad (17)$$

$$(\mathbf{B})_{mn} = \int_{-\infty}^{\infty} P_{w_\epsilon}(k_z)H_m^*(k_z)H_n(k_z)dk_z. \qquad (18)$$

Here, H_m^* denotes complex conjugate of H_m. The SNR, as expressed in Eq. (16), involves the total power of the signal and noise data, irrespectively of the direction of the signal in the data space relative to the dominant eigenvectors of the noise. This is in contrast to the detectors presented in section III-C

which aim to exploit such directional signal aspects. It is however reasonable to expect that a filter $H(k_z)$ that maximises the SNR will also be beneficial for the detection performance observed in real experiments, although no general optimality is claimed. One reason for selecting the channel weights α_m based on the SNR criterion is that it requires observations only of the noise (i.e. powder flow) statistics, and can thus be implemented in a real-time detection system. Furthermore, our empirical observations regarding the relation between the choice of α_m and the resulting detection performance indicates that this is an adequate strategy, which is also inherently adaptive to changing flow conditions.

The Rayleigh quotient in Eq. (16) is maximised by the eigenvector associated with the largest eigenvalue to the generalised eigenvalue problem

$$\mathbf{A}\boldsymbol{\alpha} = \lambda \mathbf{B}\boldsymbol{\alpha}. \tag{19}$$

Hence, by denoting the solutions to this equation as $\left(\lambda^{(i)}, \boldsymbol{\alpha}^{(i)}\right)$ with the eigenvalues arranged in descending order $\lambda^{(1)} > \cdots > \lambda^{(M)}$, the SNR-optimal channel weights are given by $\boldsymbol{\alpha} = \boldsymbol{\alpha}^{(1)}$. To compute the matrix $\mathbf{B}$, we use an estimate of the noise power spectrum obtained by expanding $P_{w_\epsilon}(k_z)$ in terms of unknown coefficients c_j and basis functions ϕ_j according to

$$P_{w_\epsilon}(k_z) = \sum_{j=-(M-1)}^{M-1} c_j \phi_j(k_z). \tag{20}$$

The basis functions $\phi_j(k_z)$ are piecewise constant with the properties $\phi_i(k_z)\phi_j(k_z) = \delta_{ij}$ (where δ_{ij} is the Kronecker delta), $\phi_j(-k_z) = \phi_j(k_z)$, and $\sum_{j=-\infty}^{\infty} \phi_j(k_z) = 1$ for all k_z, and they are defined according to

$$\phi_j(k_z) = \begin{cases} 1 & \text{if } \frac{1}{2}(\hat{k}_{j-1} + \hat{k}_j) < k_z \le \frac{1}{2}(\hat{k}_j + \hat{k}_{j+1})) \\ 0 & \text{otherwise} \end{cases} \tag{21}$$

where $\hat{k}_j$ denotes the location of the peak of $|H_{|j|+1}(k_z)|$ that occurs approximately at the frequency $(j+1)2\pi/L$ rad/m for $j \ne 0$ and at zero frequency for $j = 0$.

We seek to estimate P_{w_ϵ} from Eq. (11) using an estimate $\hat{P}_{x_m}$ for the power spectrum of the data $x_m[n]$ which is computed according to

$$\hat{P}_{x_m}(\omega) = \sum_{l=-W}^{W} \hat{r}_{x_m}[l] e^{j(\omega/F_s)l}, \tag{22}$$

where $\hat{r}_{x_m}[l]$ is the sample autocorrelation sequence of $x_m[n]$ given by

$$\hat{r}_{x_m}[l] = \frac{1}{N_{\text{tot}}} \sum_{n=0}^{N_{\text{tot}}-1-l} x_m[n+l]x_m[n]. \tag{23}$$

Here N_{tot} is the total number of samples in a measurement sequence. The coefficients c_j are computed by inserting the expansion (20) into Eq. (11) and setting the weighted residual to zero using weighting functions ϕ_i (i.e. Galerkin's method).

This yields the following over-determined system of linear equations

$$\begin{bmatrix} \mathbf{D}^{(1)} \\ \vdots \\ \mathbf{D}^{(M)} \end{bmatrix} \begin{bmatrix} c_0 \\ \vdots \\ c_{M-1} \end{bmatrix} = \begin{bmatrix} \mathbf{b}^{(1)} \\ \vdots \\ \mathbf{b}^{(M)} \end{bmatrix} \tag{24}$$

where

$$(\mathbf{D}^{(m)})_{ij} = \int_{-\infty}^{\infty} \phi_i(k_z)\phi_j(k_z)|H_m(k_z)|^2 dk_z \tag{25}$$

$$(\mathbf{b}^{(m)})_i = \int_{-\infty}^{\infty} \phi_i(\omega)\hat{P}_{x_m}(\omega)d\omega \tag{26}$$

for $i,j = 0, \ldots, (M-1)$. The weighting functions $\phi_i(\omega)$ in the ω domain are defined analogously to $\phi_i(k_z)$ in Eq. (21) using the corresponding peaks in $\hat{P}_{x_m}(\omega)$. The coefficients $c_0, \ldots, c_{M-1}$ obtained from the least-squares solution to Eq. (24) then yield the estimated permittivity spectrum via Eq. (20) using the symmetry property $c_{-j} = c_j$. The matrix $\mathbf{A}$ is computed in an analog fashion, where we use the idealised signatures $h_m(t)$ given by Eq. (2) with unit amplitudes $A_m = 1$ and apply the same pre-processing and spectrum estimation procedure as for the noise data that leads to the matrix $\mathbf{B}$.

B. Data pre-processing

We assume that complex data $w_m[n] = w_m(nT_s)$ is available at the measurement frequencies f_m, $m = 1, \ldots, M$ close to the resonant frequency of the $M = 9$ different modes. The discrete time samples $n = 0, \ldots, N-1$ are uniformly spaced in time with sampling frequency $F_s = 1/T_s = 500\,\text{Hz}$, and we assume that all noise statistics are stationary during any time interval of length NT_s. Data sequences that contain more than N samples are analyzed in a sliding-window fashion. Here, we estimate all parameters that describe the statistics of the noise (except $b_m[n]$ which is calculated according to Eq. (27), and $\hat{r}_{x_m}$ in Eq. (23) where all pre-processed data in a measurement sequence is used) based on data in an estimation window containing the samples $n = n_0, \ldots, n_0 + N - 1$ for some starting time n_0. These parameter values are used to evaluate the output of the detection algorithms in a succeeding analysis window containing the samples $n = n_0 + N, \ldots, n_0 + N + N_s - 1$. The estimation window is then successively shifted N_s samples and the above procedure is repeated, until the entire measurement sequence is covered.

The pre-processing procedure aims to map $w_m[n]$ onto a new real-valued data sequence $x_m[n]$ that mainly accounts for the variation in the material density. In particular, an increase in the real part of the effective permittivity (either due to the background material or an object) should yield a deviation in $x_m[n]$ with the same sign for all channels m, given that the dielectrics have sufficiently small losses. The conformity of the signs in the different channels is essential to obtain the correct temporal signatures when different channels are linearly combined, as described in sections III-A and III-C. The pre-processing uses data which is collected when a granular material is flowing in the sensor where no objects

are assumed to be present. We first remove the d.c. and low-frequency components by subtracting from $w_m[n]$ the moving average

$$b_m[n] = \sum_{k=0}^{K-1} g[k] w_m[n-k] \qquad (27)$$

where $g[k]$ are Hamming window coefficients. Next, we decorrelate the real and imaginary parts of $(w_m[n] - b_m[n])$ and normalise their variances by letting $\mathbf{y}[n] = \begin{bmatrix} \mathrm{Re}(w_m[n] - b_m[n]), & \mathrm{Im}(w_m[n] - b_m[n]) \end{bmatrix}^{\mathrm{T}} \in \mathbb{R}^2$ and compute the sample covariance matrix $\hat{\boldsymbol{\Sigma}}_{\mathbf{y}} = N^{-1} \sum_{n=0}^{N-1} \mathbf{y}[n] \mathbf{y}[n]^{\mathrm{T}}$. From the eigenvalue factorization $\hat{\boldsymbol{\Sigma}}_{\mathbf{y}} = \mathbf{Q} \boldsymbol{\Lambda} \mathbf{Q}^{\mathrm{T}}$ we obtain a new data representation $\mathbf{z}[n] = \boldsymbol{\Lambda}^{-1/2} \mathbf{Q}^{\mathrm{T}} \mathbf{y}[n] = \begin{bmatrix} z_1[n], & z_2[n] \end{bmatrix}^{\mathrm{T}}$. By ordering the eigenvalues according to $(\boldsymbol{\Lambda})_{11} \geq (\boldsymbol{\Lambda})_{22}$, we ensure that z_1 is associated with the direction of largest variance in w_m, which usually corresponds to variations in the material density if the material has sufficiently small losses. The desired pre-filtered data is then obtained as $x_m[n] = z_1[n]$, i.e. the largest principal component that accounts for the majority of the variability in $w_m - \mu_m$. This is done independently for all channels $m = 1, \ldots, M$. Finally, we adjust the signs according to $x_m[n] \leftarrow x_m[n] \, \mathrm{sign}\left(\sum_{n=0}^{N-1} x_1[n] x_m[n] \right)$ for $m = 2, \ldots, M$, to ensure that an increase in the effective permittivity yields a deviation in x_m which has the same sign for all channels.

C. Detection algorithm

Given the channel coefficients α_m selected by the procedure described section III-A, we combine the M channels $x_m[n]$ into a single time-sequence $x[n]$ using Eq. (13). At each time n, we vectorise W subsequent time-samples of x according to

$$\mathbf{x}[n] = [x[n-W+1], \ldots, x[n]]^{\mathrm{T}} \in \mathbb{R}^W. \qquad (28)$$

The length of the analysis window is set to $W = \lceil 1.1 F_s L/v \rceil$ to include one transit time through the sensor with some margin at the flow speed v. The flow speed is estimated based on the non-zero peak locations ω_m^{peak} in the power spectra $\hat{P}_{x_m}(\omega)$ and the corresponding non-zero peak locations k_m^{peak} of $|H_m(k_z)|$ according to $\hat{v}_m = \omega_m^{\mathrm{peak}}/k_{z,m}^{\mathrm{peak}}$ for each mode $m = 2, \ldots, M$, and a single flow speed is computed as the average $v = (M-1)^{-1} \sum_{m=2}^{M} \hat{v}_m$. The detection problem is formulated as a hypothesis test according to

$$\mathcal{H}: \quad \mathbf{x}[n] = \mathbf{v}[n] \qquad (29)$$
$$\mathcal{K}: \quad \mathbf{x}[n] = \mathbf{s}[n] + \mathbf{v}[n] \qquad (30)$$

with null hypothesis $\mathcal{H}$ (no object present) and alternative hypothesis $\mathcal{K}$ (object present). Here, the noise $\mathbf{v}[n]$ models the response due to permittivity variations in the granular flow as well as measurement noise, and the target signal $\mathbf{s}[n]$ represents the waveforms caused by the passage of an object. The target signal is not completely known but contains unknown parameters to be estimated from data. Therefore, we apply the generalised likelihood ratio test (GLRT) where

all unknown parameters are replaced by their maximum-likelihood (ML) estimates [26]. This yields

$$T_{\mathrm{GLRT}}(\mathbf{x}[n]) = \log \left(\frac{p(\mathbf{x}[n] | \mathcal{K})}{p(\mathbf{x}[n] | \mathcal{H})} \right) \underset{\mathcal{H}}{\overset{\mathcal{K}}{\gtrless}} \eta, \qquad (31)$$

where p is the probability density function of the data under each hypothesis. Hence, we accept the alternative hypothesis $\mathcal{K}$ if the test statistic T_{GLRT} exceeds the threshold η. We make the assumption that the noise is zero-mean multivariate normal distributed according to $\mathbf{v}[n] \sim \mathcal{N}(\mathbf{0}, \boldsymbol{\Sigma})$, which is reasonable given the pre-processing described in section III-B. Since the entries of $\mathbf{v}[n]$ are subsequent time-samples, the covariance matrix $\boldsymbol{\Sigma}$ is an autocorrelation matrix with a Toeplitz structure that is given by

$$\boldsymbol{\Sigma} = \begin{bmatrix} r_v[0] & \ldots & r_v[W-1] \\ \vdots & \ddots & \vdots \\ r_v[W-1] & \ldots & r_v[0] \end{bmatrix} \qquad (32)$$

where $r_v[l] = E[v[n+l]v[n]]$ is the autocorrelation sequence for the noise $v[n]$. We compute an estimate $\hat{\boldsymbol{\Sigma}}$ of the true covariance matrix $\boldsymbol{\Sigma}$ by replacing $r_v[l]$ in Eq. (32) by the corresponding sample autocorrelations

$$\hat{r}_x[l] = \frac{1}{N} \sum_{n=0}^{N-1-k} x[n+l] x[n], \qquad (33)$$

based on data $x[n]$ collected when a flowing granular material is assumed present in the sensor without any objects. The estimated covariance matrix $\hat{\boldsymbol{\Sigma}}$ (which is not an ML estimate) is used in both PDF:s in the likelihood ratio. Hence, Eq. (31) is the correct GLRT only if the estimated covariance matrix is assumed to be the true covariance matrix, so that the remaining parameters to be estimated from data are those describing the signal $\mathbf{s}[n]$.
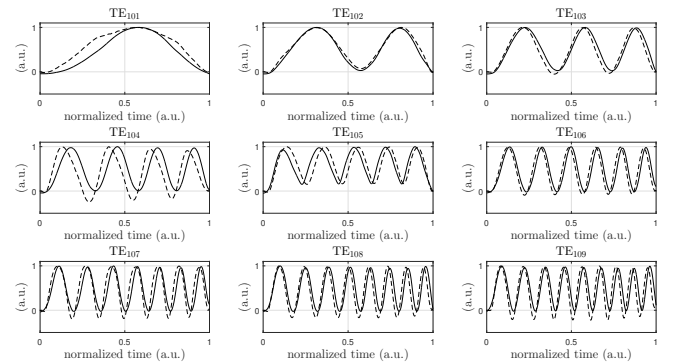

Figure 5. Target waveforms observed by each mode due to 6 mm Delrin spheres (solid curves) and 6 mm steel spheres (dashed curves) falling through the sensor.

The target signal $\mathbf{s}[n]$ is constructed from the waveforms obtained by the averaged results from 50 repeated measurements on a single object falling through the sensor. These waveforms, which are slightly different for metal and dielectric objects as discussed in section II-B, are shown in Fig. 5 where the effect of acceleration is discernible. A comparison with the theoretical waveforms in Fig. 4(a) and Fig. 11 shows good

agreement regarding the principal shape and periodicity. To account for an unknown polarisability and speed of a real object, we parametrise the target signal using the following model

$$\mathbf{s}(\lambda, \theta)[n] = \mathbf{H}_\lambda \theta[n] \in \mathbb{R}^W, \tag{34}$$

where $\mathbf{H}_\lambda = \sum_{m=1}^M \alpha_m \mathbf{s}_m^\lambda \in \mathbb{R}^{W \times 1}$ and $\theta[n] \in \mathbb{R}$. Here, λ is a parameter that controls the duration of the target waveform and hence the speed of the object according to

$$\mathbf{s}_m^\lambda = [(\mathbf{0}^{\lfloor (1-\lambda)W \rfloor})^{\mathrm{T}} \ (\tilde{\mathbf{s}}_m^\lambda)^{\mathrm{T}}]^{\mathrm{T}} \in \mathbb{R}^W \tag{35}$$

where $\mathbf{0}^P$ is a column vector with P zeros and $\tilde{\mathbf{s}}_m^\lambda$ is a vector that contain $\lceil \lambda W \rceil$ uniformly spaced samples of the measured target waveform for mode m. The ML estimates of θ and λ at each time,

$$\hat{\theta}, \hat{\lambda} = \arg\max_{\theta, \lambda} p(\mathbf{x}[n] | \mathcal{K}; \theta, \lambda) \tag{36}$$

are computing by a two-step procedure where we first fix λ and solve for the resulting $\hat{\theta}$ (which enters linearly in the signal model) according to

$$\hat{\theta}_\lambda[n] = (\mathbf{H}_\lambda^{\mathrm{T}} \hat{\mathbf{\Sigma}}^{-1} \mathbf{H}_\lambda)^{-1} \mathbf{H}_\lambda^{\mathrm{T}} \hat{\mathbf{\Sigma}}^{-1} \mathbf{x}[n]. \tag{37}$$

Next, we insert the estimate $\hat{\theta}_\lambda$ into the likelihood function that we subsequently maximize with respect to λ by means of grid search over a finite number of values $\{\lambda_q\}_{q=1}^Q$ which are selected to account for an expected range of object speeds. For fixed λ, the estimated signal is given by $\hat{\mathbf{s}}_\lambda[n] = \mathbf{H}_\lambda \hat{\theta}_\lambda[n] = \mathbf{P}_\lambda \mathbf{x}[n]$, where

$$\mathbf{P}_\lambda = \mathbf{H}_\lambda (\mathbf{H}_\lambda^{\mathrm{T}} \hat{\mathbf{\Sigma}}^{-1} \mathbf{H}_\lambda)^{-1} \mathbf{H}_\lambda^{\mathrm{T}} \hat{\mathbf{\Sigma}}^{-1} \tag{38}$$

is a projection matrix that projects onto the subspace of $\mathbb{R}^W$ spanned by the single column of $\mathbf{H}_\lambda$, i.e. the expected target signal. If we consider only the data-dependent part of the log-likelihood ratio in Eq. (31), the detection criterion can then be written

$$T_{\mathrm{MF}}(\mathbf{x}[n]) = (\mathbf{P}_{\hat{\lambda}} \mathbf{x}[n])^{\mathrm{T}} \hat{\mathbf{\Sigma}}^{-1} (\mathbf{P}_{\hat{\lambda}} \mathbf{x}[n]) \underset{\mathcal{H}}{\overset{\mathcal{K}}{\gtrless}} \eta'. \tag{39}$$

Here, we have used the relations $\mathbf{x}^{\mathrm{T}} \hat{\mathbf{\Sigma}}^{-1} \hat{\mathbf{s}}_\lambda = \hat{\mathbf{s}}_\lambda^{\mathrm{T}} \hat{\mathbf{\Sigma}}^{-1} \hat{\mathbf{s}}_\lambda$ and $\hat{\mathbf{s}}_\lambda = \mathbf{P}_\lambda \mathbf{x}$. The detection criterion (39) can be viewed as an incoherent noise-whitening matched filter whose output compared to a threshold η' determines the detection decision. We therefore refer to this detector as a matched filter detector (MF). An interpretation of the test statistic in Eq. (39) is that we first compute the projection of the data in the direction of the expected target signal, and subsequently calculate the power of this projection whitened with respect to the noise statistics. Hence, this detector yields a high output value if the data contains the expected target signal, especially if this signal points in a direction in $\mathbb{R}^W$ where the noise is weak.

A different approach to the detection problem is to let the detection be based entirely on a measure of the deviation from the noise characteristics, without incorporating any directed information about the expected target waveforms. This approach can be followed by increasing the dimensionality of the signal

subspace (e.g by adding columns to $\mathbf{H}_\lambda$) so that the projection matrix in Eq. (38) becomes a full-rank matrix that maps any data vector $\mathbf{x}[n]$ onto itself. The test-statistic (i.e. the data-dependent part of the log-likelihood ratio) then becomes

$$T_{\mathrm{TPD}} = \mathbf{x}^{\mathrm{T}}[n] \hat{\mathbf{\Sigma}}^{-1} \mathbf{x}[n]. \tag{40}$$

We refer to this detector as a temporal power detector (TPD) since the test statistic is the power of the noise-whitened temporal signal $\hat{\mathbf{\Sigma}}^{-1/2} \mathbf{x}[n]$. This detector is sensitive to any temporal variation in the data that differs from the noise statistics as prescribed by $\hat{\mathbf{\Sigma}}$, and therefore requires no prior knowledge about the actual target waveforms. This detector can be particularly effective if the object travels at a higher speed than the background material which yields unusual high-frequency components in the target waveform.

Yet another option is to use a detector that exploits the instantaneous correlations between different channels but ignores all aspects of the temporal variation. By forming a data vector from different channels at a single snapshot according to $\mathbf{x}_{\mathrm{SPD}}[n] = [x_1[n], \ldots, x_M[n]]^{\mathrm{T}}$, a spatial power detector (SPD) can be formulated with the test statistic

$$T_{\mathrm{SPD}}(\mathbf{x}_{\mathrm{SPD}}[n]) = \mathbf{x}_{\mathrm{SPD}}^{\mathrm{T}}[n] \hat{\mathbf{\Sigma}}_{\mathrm{SPD}}^{-1} \mathbf{x}_{\mathrm{SPD}}[n] \tag{41}$$

where $\hat{\mathbf{\Sigma}}_{\mathrm{SPD}}$ is the sample covariance matrix of $\mathbf{x}_{\mathrm{SPD}}$. This is similar to the detector used in [24] although, here, the measured data is subject to another type of pre-processing. The term spatial here refers to the aspect that the different channels (i.e. modes) have different spatial sensitivity patterns. The detection performance of the three detectors presented in the foregoing are compared in section IV.

IV. RESULTS

A. Experimental setup

We evaluate the performance of our detection system using an experimental setup shown in Fig. 6. The granulate is stored in a conical hopper made of stainless steel and the granules are discharged through the hopper outlet where an adjustable valve controls the mass flow rate. The granulate is directed by a funnel into a vertical buffer pipe where the main acceleration occurs, and then down the sensor. The funnel is also used to direct the test objects down the pipe. The test objects are stored in holes in a perforated disc that is rotated step-wise using a stepper-motor, and each object is released into the flow when its hole is aligned with a hole in the underlying slab. The time at which each object is released is thereby known with high accuracy, which makes it possible to reliably predict a time interval where the object is present in the sensor. The powder and the objects are collected at the bottom end of the sensor in a bucket standing on a scale that measures the mass repeatedly over time so that the instantaneous mass flow can be obtained by time differentiation of the total mass. The microwave transceiver described in section II-C measures repeatedly S_{21} between the sensor ports 1 and 2 and is controlled by a PC. This setup allows us to study the detection capabilities under representative industrial conditions where granulates are flowing by the aid of gravity.
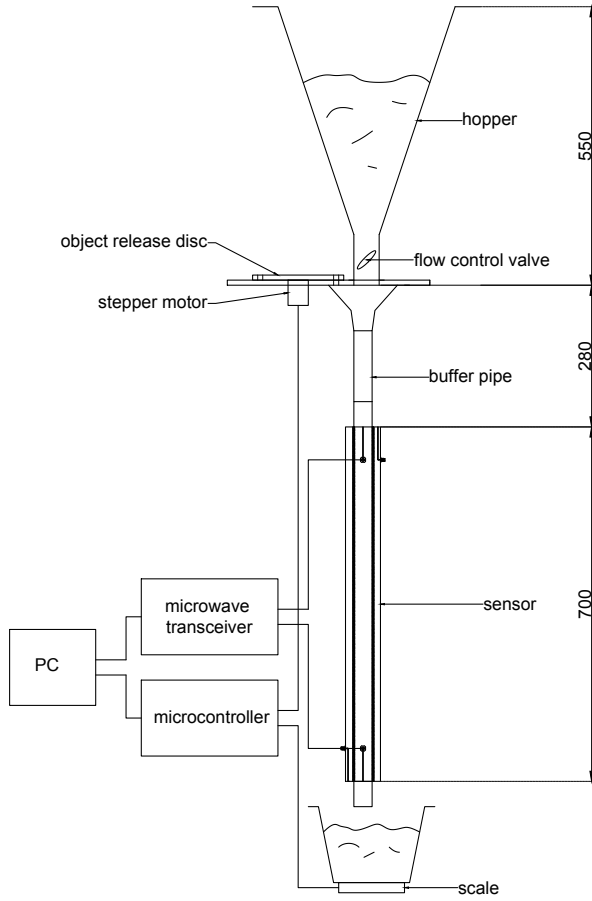
Figure 6. Experimental setup including hopper, object release system, sensor and microwave measurement electronics. All dimensions are in millimetres.

B. Detection performance evaluation

The granular materials used to study the detection performance are (i) spherical pellets of microcrystalline cellulose (MCC) with diameters in the range 700-1000 μm (Cellets® 700, Harke Pharma GmbH) and (ii) glass beads (SiO₂-dominated) with diameter range 200-400 μm intended for sand blasting. Both granulates are discharged at a rate of 100 kg/h. We use test objects that consist of steel and Delrin (polyoxymethylene), respectively, which are spherical with diameters 2, 4, 6 and 8 mm. We also study white pepper seeds as test objects, which are approximately spherical with an average diameter of 4 mm.

The target waveforms used in the matched filter detector are obtained from the measured signatures shown in Fig. 5 and we use the dielectric-response waveforms when Delrin or pepper objects are tested, and metal-response waveforms when steel objects are tested. Investigations show that by choosing the right waveform (dielectric or metal) for the object being tested yields a small but consistent improvement in the detection performance. Each measurement sequence consists of discharging one completely filled hopper which takes approximately 3 minutes. During this time, 70-100 identical test objects are released into the flow with 2 seconds between subsequent objects. We define a test interval from 0.2 to 0.8

seconds after each object is released, during which the object is assumed to have entered and exited the sensor. Similarly, we define a set of validation intervals of the same length (0.6 s) during which no object is assumed present. A positive detection made during a test interval is therefore classified as correct and a positive detection made during a validation interval is classified as incorrect. For a given detector and a given threshold, we compute the detection and false-alarm rates as the ratios of the number of true and false detections to the total number of test and validation windows, respectively.

C. Data illustration

Here we present intermediate results to illustrate the steps in the pre-processing and detection algorithms. Figure 7 shows the distribution of the raw data $w_m[n]$ in the complex plane together with an ellipse that represents the covariance matrix of $\mathrm{Re}[w_m]$ and $\mathrm{Im}[w_m]$, as described Section III-B. If the semi-axes of this ellipse are represented by the local coordinate axes u_1 and u_2, then the pre-processed data $x_m[n]$ is the variance-normalised projection of the data $(w_m[n]-b_m)$ in the direction of u_1 (i.e. the first principal component), where b_m is the mean of w_m. The resulting pre-processed data $x_m[n]$ is shown as a function of time in Fig. 8. For low-loss materials, an increase in the material density and hence in the effective permittivity yields a variation in w_m mainly in the direction of u_1 (and thus in x_m) as indicated in Fig. 7.

The sample autocorrelations $\hat{r}_{x_m}[l]$ and the associated power spectra $\hat{P}_{x_m}(\omega)$, which are calculated according to Eqs. (23) and (22), are shown in Fig. 9 for flowing MCC granules without any objects. The average flow speed v among modes 2-9 (estimated as described in section III-C) varies between 3.4 m/s and 3.7 m/s for different measurement sequences for both MCC and glass beads. The average particle volume fraction can be calculated as

$$\nu = \frac{\dot{m}}{Av(\rho_\mathrm{p} - \rho_\mathrm{air})} \quad (42)$$

where $\dot{m} = 100$ kg/h is the particle mass flow rate, $A = \pi(D/2)^2$ is the cross-section area of the pipe and $\rho_\mathrm{air} = 1.2$ kg/m³ is the assumed density of air. Given the solid mass densities $\rho_\mathrm{p} = 1300$ kg/m³ for MCC and $\rho_\mathrm{p} = 2400$ kg/m³ for glass (obtained by measuring the bulk density and assuming random close-pack with volume fraction 0.64), we obtain a volume fraction during flow of approximately 0.6 % for the MCC particles and 0.3 % for the glass beads.

Given the data spectra $\hat{P}_{x_m}$ shown in Fig. 9, we estimate the permittivity spectra $\hat{P}_{s_\epsilon}$ and $\hat{P}_{w_\epsilon}$ of a small dielectric object and of the powder flow, respectively, as described in section III-A, and these estimates are shown in Fig. 10. Here, we notice that the spectrum of the object's permittivity is essentially flat, as expected. Furthermore, we notice that $\hat{P}_{w_\epsilon}$ is relatively small at low frequencies ($k_z \approx 0$) and at the higher frequencies corresponding approximately to the passband for mode 7-9. From the permittivity spectra, we compute the SNR-optimized channel weights α_m as described in section III-A which are presented in Tab. I. The sensitivity $h(z)$ and the associated transfer function $H(k_z)$ of the combined spatial filter obtained from these channel weights is shown in Fig. 11.

It is seen that the combined filter has a large gain at the spatial frequencies where $\hat{P}_{w_\epsilon}$ is small in comparison with $\hat{P}_{s_\epsilon}$, which makes sense.
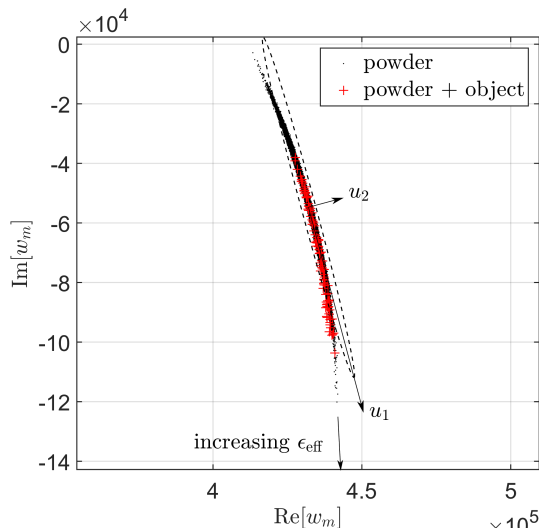

Figure 7. Distribution of the raw data w_m in the complex plane for mode $m = 9$ due to powder and due a white pepper seed object. The dashed ellipse represent the covariance matrix of the variations in $\mathrm{Re}[w_m]$ versus $\mathrm{Im}[w_m]$ around their mean values, and the major axes of the ellipse are represented by the local coordinate axes u_1 and u_2.
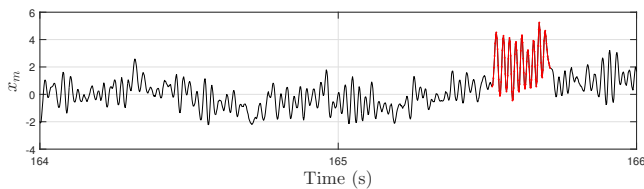

Figure 8. Pre-processed data $x_m[n]$ versus time for mode $m = 9$ with a white pepper seed present at the highlighted time interval.

Table I
SNR-OPTIMAL CHANNEL WEIGHTS FOR MCC PELLETS FLOWING AT 100 KG/H.

α_1	α_2	α_3	α_4	α_5	α_6	α_7	α_8	α_9
0.01	0.02	0.02	0.03	0.04	0.06	0.12	0.49	-0.86

D. Detection results

We compare the detection performance of the matched filter detector in comparison with the temporal and spatial power detectors, based on measurement sequences that each involves 70-100 object passages with a total duration of approximately 3 minutes. We analyse the data in blocks of length $N = 5000$ samples (10 seconds) that are successively shifted $N_s = 500$ samples, where all parameters describing the statistics of the noise (except $b_m[n]$) are re-evaluated for each block. The length of the Hamming-window in Eq. (27) is set to $K = 500$ samples (1 second). Furthermore, the estimated flow speed determines the length W of the analysis window according to $W = \lceil 1.1 F_s L/v \rceil = 114$ samples (0.23 seconds) if the flow speed is $v = 3.4\,\mathrm{m/s}$.
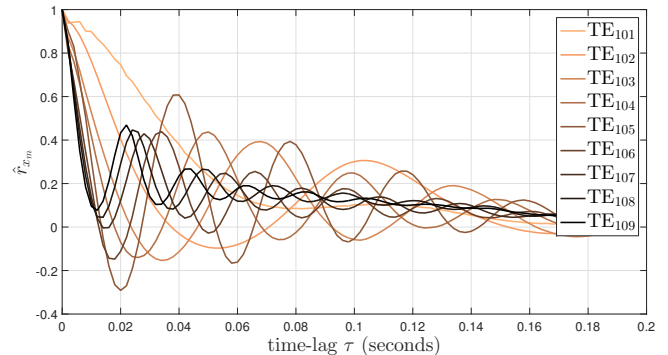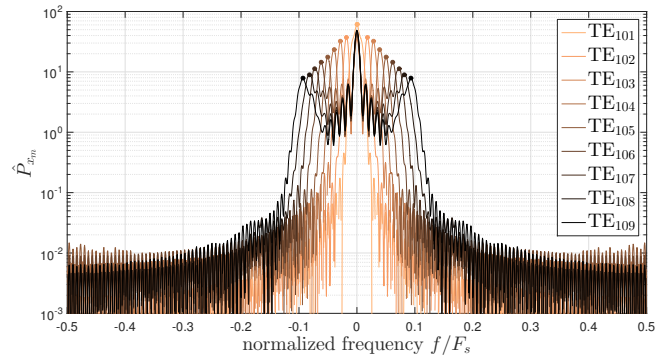
Figure 9. (a) Sample autocorrelations $\hat{r}_{x_m}$ and (b) power spectra $\hat{P}_{x_m}$ for each individual mode $m = 1, \ldots, 9$, based on a data sequence where MCC pellets are flowing at $100\,\mathrm{kg/h}$ with no objects present. The peaks in the spectra are marked by filled circles.
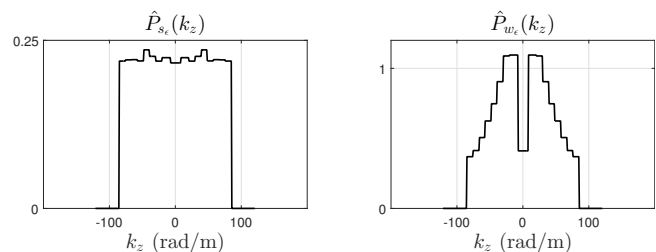

Figure 10. Estimated permittivity spectra $\hat{P}_{s_\epsilon}$ (left figure) and $\hat{P}_{w_\epsilon}$ (right figure) for a dielectric object and for MCC pellets flowing at $100\,\mathrm{kg/h}$, respectively.

The detection performance can be characterised by the receiver operating characteristics (ROC) where P_D is plotted versus P_{FA} for all values of the threshold. Figure 12 shows the ROC for $4\,\mathrm{mm}$ steel objects in MCC granules, where we notice that the matched filter detector performs clearly better than the power detectors. The area under the ROC-curve (AUC) is here used as a summary statistic to characterize the overall detector performance [27] where AUC= 1 corresponds to perfect classification and AUC= 0.5 is equivalent to random guessing. The detection performance in terms of AUC is summarised in Table II for the available test objects in MCC and glass granulates, where the uncertainty in the AUC is calculated by means of bootstrapping using 10'000 bootstrap resamples [28]. The interval limits presented in the table are obtained as the points where the cumulative distribution function (CDF) of the
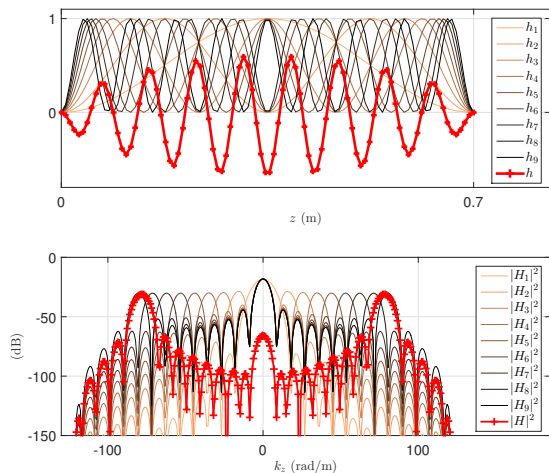
Figure 11. Spatial sensitivity for modes 1-9 and the combined spatial filter obtained from the channel weights α_m presented in Table I, in the spatial domain (top figure) and in the spatial frequency domain (bottom figure).
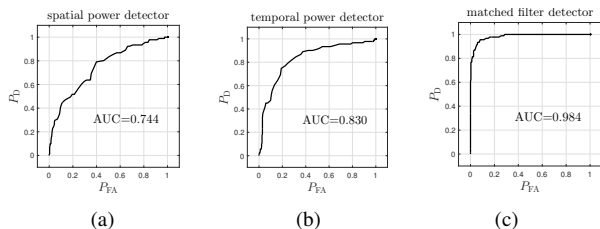

Figure 12. ROC curves for the detection of 2 mm steel balls in glass beads flowing at 100 kg/h, for (a) the spatial power detector, (b) the temporal power detector, and (c) the matched filter detector. The result is based on 92 object passage events during 235 seconds of powder flow.

Table II
AREA UNDER THE ROC-CURVE FOR COMBINATIONS OF GRANULATE AND TEST OBJECT, USING THE SPATIAL POWER DETECTOR (SPD), TEMPORAL POWER DETECTOR (TPD) AND MATCHED FILTER DETECTOR (MF). THE INTERVAL LIMITS ARE THE AUC-VALUES THAT CORRESPOND TO THE 10% AND 90% LEVELS OF THE EMPIRICAL BOOTSTRAP CDF.

	MCC pellets (100 kg/h)		
	SPD	TPD	MF
steel 4mm	0.996 - 0.999	0.999 - 1.000	0.999 - 1.000
steel 2mm	0.518 - 0.622	0.467 - 0.572	0.525 - 0.629
delrin 8mm	1.000 - 1.000	1.000 - 1.000	1.000 - 1.000
delrin 6mm	1.000 - 1.000	0.999 - 1.000	1.000 - 1.000
delrin 4mm	0.750 - 0.825	0.559 - 0.648	0.837 - 0.895
delrin 2mm	0.469 - 0.564	0.472 - 0.566	0.512 - 0.604
pepper 4mm	0.843 - 0.902	0.844 - 0.902	0.948 - 0.981

	glass beads (100 kg/h)		
	SPD	TPD	MF
steel 4mm	1.000 - 1.000	1.000 - 1.000	1.000 - 1.000
steel 2mm	0.705 - 0.781	0.796 - 0.863	0.977 - 0.990
delrin 8mm	1.000 - 1.000	1.000 - 1.000	1.000 - 1.000
delrin 6mm	1.000 - 1.000	1.000 - 1.000	1.000 - 1.000
delrin 4mm	0.988 - 1.000	0.988 - 0.997	1.000 - 1.000
delrin 2mm	0.505 - 0.601	0.504 - 0.594	0.579 - 0.665
pepper 4mm	1.000 - 1.000	0.999 - 1.000	1.000 - 1.000

V. CONCLUSION

We present a microwave measurement system for detecting dielectric and metal objects in flowing granular materials. The system comprises a resonant cavity sensor for measurements in pipes, a fast-sampling microwave transceiver, and a signal processing algorithm for object detection and estimation of statistical flow properties. The sensor supports nine resonant modes which act as periodic spatial filters for the permittivity of the material in the pipe. We present a matched filter detection algorithm that incorporates the statistics of the noise due to material density fluctuations, and pre-recorded target waveforms arising due to the passage of an object.

We present a pre-processing procedure that utilises the stochastic variation of the background medium to remove the effect of an uncalibrated measurement instrument. The pre-processed data is obtained from the first principal component of the complex S-parameter data, which is used as a real-valued input to the detection algorithms. We also present a method for estimating the power spectrum of a dielectric particle flow as function of spatial frequency. Based on these estimates, we combine the resonant modes such that the signal-to-noise ratio is maximised.

Experiments that involve repeated observations of up to 100 identical test objects in granular materials that flow by the aid of gravity, are used to assess the detection performance. For a granulate consisting of microcrystalline cellulose pellets flowing at 100 kg/h, we achieve perfect detection of metal spheres down to 4 mm in diameter and Delrin spheres down to 6 mm in diameter. For glass beads flowing at 100 kg/h, we obtain good detection of metal spheres down to 2 mm and of Delrin spheres down to 4 mm in diameter. The matched filter detector is shown to perform uniformly better than two reference power detectors. The signal processing algorithm is based on linear processing which makes it straight-forward to implement in a real-time detection system, possibly using uncalibrated low-cost microwave measurement hardware.

empirical bootstrap distribution for the AUC attains the values 0.1 and 0.9. Here, we notice that the matched filter performs uniformly better than the other detectors. The difference is most clear for the steel objects, where also the temporal power detector performs better than the spatial power detector. This may be due to that the steel objects obtain a higher fall speed due to their higher mass density. This, and possibly the fact that metal objects give rise to different waveforms than dielectric objects as shown in section III-C, yields object waveforms that are more distinguishable relative to the density fluctuations of the dielectric powder.

The smallest metal objects that can be reliably detected in this paper are significantly larger than the detection limit for commercial metal detectors [29]. For dielectric objects, however, we are not aware of any publication that presents quantitative detection results for flowing granular materials except the previous publications by the authors [24], [30]. In [31] and [32], X-ray imaging is used for detecting various metal and dielectric objects in static material samples. Although significant improvements by multi-modal X-ray imaging is demonstrated in [32], it is clear that low-density objects (plastics, wood, rubber) are particularly challenging to detect by X-ray, especially if the background material has significant texture.

REFERENCES

[1] J Duran. *Sands, Powders, and Grains: An Introduction to the Physics of Granular Materials*. Springer, 2000.

[2] M Abou-Khousa, A Al-Durra, and K Al-Wahedi. Microwave sensing system for real-time monitoring of solid contaminants in gas flows. *IEEE Sensors J.*, 15(9):5296–5302, 2015.

[3] M Graves, A Smith, and B Batchelor. Approaches to foreign body detection in foods. *Trends in Food Science & Technology*, 9(1):21–27, 1998.

[4] D L Black, M Q McQuay, and M P Bonin. Laser-based techniques for particle-size measurement: A review of sizing methods and their industrial applications. *Progress in Energy and Combustion Science*, 22(3):267–306, 1996.

[5] R M Carter, Y Yan, and P Lee. On-line nonintrusive measurement of particle size distribution through digital imaging. *IEEE Trans. Instrum. Meas*, 55(6):2034–2038, 2006.

[6] L Gao, Y Yan, R M Carter, D Sun, P Lee, and C Xu. On-line particle sizing of pneumatically conveyed biomass particles using piezoelectric sensors. *Fuel*, 113:810–816, 2013.

[7] G P Hancke and R Malan. A modal analysis technique for the on-line particle size measurement of pneumatically conveyed pulverized coal. *IEEE Trans. Instrum. Meas*, 47(1):114–122, 1998.

[8] Y Hu, L Wang, X Huang, X Qian, L Gao, and Y Yan. On-line sizing of pneumatically conveyed particles through acoustic emission detection and signal analysis. *IEEE Trans. Instrum. Meas.*, 64(5):1100–1109, 2015.

[9] Y Shirakawa, Y Matsuo, J Ohno, S Watanabe, and H Yashiro. On-line measurement of particle size by microwave technology. *Nippon Steel Technical Report*, 49:9–14, 1991.

[10] D Sun, Y Yan, R M Carter, L Gao, G Lu, G Riley, and M Wood. On-line nonintrusive detection of wood pellets in pneumatic conveying pipelines using vibration and acoustic sensors. *IEEE Trans. Instrum. Meas.*, 63(5):993–1001, 2014.

[11] K Folgerø, T Friisø, J Hilland, and T Tjomsland. A broad-band and high-sensitivity dielectric spectroscopy measurement system for quality determination of low-permittivity fluids. *Meas. Sci. Technol.*, 6(7):995–1008, 1995.

[12] A W Kraszewski, T-S You, and S O Nelson. Microwave resonator technique for moisture content determination in single soybean seeds. *IEEE Trans. Instrum. Meas.*, 38:79–84, 1989.

[13] S Trabelsi and S O Nelson. Nondestructive sensing of physical properties of granular materials by microwave permittivity measurement. *IEEE Trans. Instrum. Meas.*, 55(3):953–963, 2006.

[14] J Sheen. Comparisons of microwave dielectric property measurements by transmission/reflection techniques and resonance techniques. *Meas. Sci. Technol.*, 20(4):042001, 2009.

[15] S Kobayashi and S Miyahara. A particulate flow meter using microwaves. In *Proc. IMEKO*, pages 197–204, Prague, 1985.

[16] A Penirschke and R Jakoby. Microwave mass flow detector for particulate solids based on spatial filtering velocimetry. *IEEE Trans. Microw. Theory Techn.*, 56(12):3193–3199, 2008.

[17] Y Yan, B Byrne, S Woodhead, and J Coulthard. Velocity measurement of pneumatically conveyed solids using electrodynamic sensors. *Meas. Sci. Technol.*, 6(5):515–537, 1995.

[18] Y Bertho, F Giorgiutti-Dauphiné, T Raafat, E J Hinch, H J Herrmann, and J P Hulin. Powder flow down a vertical pipe: the effect of air flow. *Journal of Fluid Mechanics*, 459:317–345, 2002.

[19] D Pozar. *Microwave Engineering*. John Wiley & Sons, 2 edition, 1998.

[20] Comsol Multiphysics. http://www.comsol.com, 2018.

[21] R F Harrington. *Time-Harmonic Electromagnetic Fields*. McGraw-Hill, 1961.

[22] A Sihvola. *Electromagnetic Mixing Formulas and Applications*. The Institution of Engineering and Technology, 1999.

[23] Y Aizu and T Asakura. Principles and development of spatial filtering velocimetry. *Applied Physics B*, 43(4):209–224, 1987.

[24] J Nohlert, T Rylander, and T McKelvey. Microwave measurement system for detection of dielectric objects in powders. *IEEE Trans. Microw. Theory Techn.*, 64(11):3851–3863, November 2016.

[25] E K Miller. Model-based parameter estimation in electromagnetics. Part I. Background and theoretical development. *IEEE Antennas and Propagation Magazine*, 40(1):42–52, 1998.

[26] S M Kay. *Fundamentals of Statistical Signal Processing: Detection Theory*. Prentice Hall, 1998.

[27] T Fawcett. An introduction to ROC analysis. *Pattern Recognition Letters*, 27(8):861–874, 2006.

[28] A M Zoubir and D R Iskander. *Bootstrap Techniques for Signal Processing*, chapter 2.1, pages 11–14. Cambridge University Press, 2004.

[29] Metal detection solutions: Powder and granular product applications. Mettler-Toledo, http://www.mt.com/metaldetection, 2018.

[30] J Nohlert, T Rylander, and T McKelvey. Matched filter for microwave-based detection of dielectric objects in powders. In *Proc. IEEE Int. Instrum. Meas. Technol. Conf. (I2MTC)*, pages 1–6, 2017.

[31] J-S Kwon, J-M Lee, and W-Y Kim. Real-time detection of foreign objects using X-ray imaging for dry food manufacturing line. In *Consumer Electronics, 2008. ISCE 2008. IEEE International Symposium on*, 2008.

[32] H Einarsdóttir, M J Emerson, L H Clemmensen, K Scherer, K Willer, M Bech, R Larsen, B K Ersbøll, and F Pfeiffer. Novelty detection of foreign objects in food using multi-modal x-ray imaging. *Food Control*, 67:39–47, 2016.